Letter

Nonequilibrium two-particle self-consistent approach

Olivier Simard and Philipp Werner
Department of Physics, University of Fribourg, 1700 Fribourg, Switzerland

We present the nonequilibrium implementation of the two-particle self-consistent (TPSC) approach, which has been shown to provide a reliable equilibrium description of interacting lattice systems in the weak- and intermediate-correlation regime. This method captures the effects of local and nonlocal correlations in two- and higher-dimensional systems and satisfies the Mermin-Wagner theorem. We demonstrate the versatility of nonequilibrium TPSC with calculations of the time-dependent spin and charge response functions and the evolution of effective temperatures extracted from different correlation functions, after interaction ramps in the two-dimensional Hubbard model.

Introduction. Nonlocal correlations play an important role in low-dimensional lattice systems and in the vicinity of phase transitions or crossovers [1–6], but calculating the single- and two-particle correlations in a consistent manner is a challenging task. While strong local or short-ranged correlations can be captured by Dynamical Mean Field Theory (DMFT) [7] and its cluster extensions [6], the study of long-ranged correlations requires diagrammatic extensions such as the Dynamical Vertex Approximation (DΓA) [8] or Dual Boson (DB) [9] methods. In the weak-to-intermediate correlation regime, the GW method [10], T-matrix approach [11], or Fluctuation Exchange Approximation (FLEX) [12] are often used, but their suitability for model calculations has been questioned [13] in a systematic comparison to diagrammatic Monte Carlo results [14]. Much more convincing results have recently been demonstrated in benchmarks [15,16] of the Two-Particle Self-Consistent (TPSC) approach [17,18], which ensures consistency between one-particle and two-particle quantities and satisfies the Mermin-Wagner theorem. This makes TPSC appealing for the study of lattice systems in dimension $D \geqslant 2$. TPSC captures the pseudo-gap physics [19] in the 2D Hubbard model and the growth of antiferromagnetic correlations in the renormalized classical regime, where the antiferromagnetic correlation length becomes larger than the de Broglie wave length. It can also be extended to treat symmetry-broken states [20], two-particle vertex corrections [2], as well as multi-orbital [21] and extended Hubbard-like systems [16]. Moreover, TPSC has been successfully combined with Density Functional Theory input [22] and with DMFT [5].

Describing the interplay between different types of correlations in out-of-equilibrium states adds another layer of complexity. Several of the above-mentioned equilibrium techniques have over the last years been adapted to nonequilibrium setups [23–37], but the development of accurate, yet computationally efficient nonequilibrium methods for two- and three-dimensional lattice systems remains a challenging research frontier. Here, we introduce the nonequilibrium TPSC

method as a powerful addition to the existing toolset, especially in the moderate-correlation regime. We describe the implementation on the Kadanoff-Baym contour and demonstrate the usefulness of the scheme with interaction quenches in the two-dimensional Hubbard model.

Model and methods. We consider the single-band Hubbard model on a D-dimensional lattice

$$\hat{\mathcal{H}}(t) = -\sum_{i,j,\sigma} t_{i,j}^{\mathrm{hop}} (\hat{c}_{i,\sigma}^{\dagger} \hat{c}_{j,\sigma} + \mathrm{H.c.})$$
$$+ U(t) \sum_i \hat{n}_{i,\uparrow} \hat{n}_{i,\downarrow} - \mu \sum_i (\hat{n}_{i,\uparrow} + \hat{n}_{i,\downarrow}), \quad (1)$$

where $t_{i,j}^{\mathrm{hop}}$ denotes the hopping amplitude, and i, j refer to lattice sites. The spin is denoted by $\sigma \in \{\uparrow, \downarrow\}$, and $\hat{c}_{i,\sigma}^{(\dagger)}$ are the annihilation (creation) operators for site i. $\hat{n}_{i\sigma} = \hat{c}_{i,\sigma}^{\dagger} \hat{c}_{i,\sigma}$ is the number operator, $U(t)$ is the local Hubbard repulsion, and μ the chemical potential. In the applications, we will show results for a two-dimensional lattice with nearest-neighbor hopping t_{hop} and use t_{hop} as the unit of energy ($\hbar/t_{\mathrm{hop}}$ as the unit of time). We set $\hbar$, k_B, the electric charge e, and the lattice spacing equal to unity.

The single- and two-particle correlation functions in TPSC are derived from the following ansatz for the Luttinger-Ward functional Φ [17,18],

$$\Phi[\mathcal{G}] = \frac{1}{2} \int_{\mathcal{C}} \mathrm{d}z \sum_{\sigma} \mathcal{G}_{\sigma}(z, z^+) \Gamma_{\sigma,\sigma}(z) \mathcal{G}_{\sigma}(z, z^+)$$
$$+ \frac{1}{2} \int_{\mathcal{C}} \mathrm{d}z \sum_{\sigma} \mathcal{G}_{\sigma}(z, z^+) \Gamma_{\sigma,-\sigma}(z) \mathcal{G}_{-\sigma}(z, z^+), \quad (2)$$

where $\mathcal{C}$ represents the Kadanoff-Baym (KB) contour [38], $z \in \mathcal{C}$ and z^+ is infinitesimally *later* than z in the contour ordering. $\mathcal{G}$ represents the one-body Green's function and Γ the local irreducible vertices in the particle-hole channel (longitudinal and transversal). The self-energy functional $\Sigma[\mathcal{G}]$ can be derived from $\Phi[\mathcal{G}]$ as $\Sigma_{ij}(z, z') = \frac{\delta \Phi[\mathcal{G}]}{\delta \mathcal{G}_{ji}(z', z)}$. The

irreducible vertex in the spin channel Γ^{sp} is defined as $\Gamma^{\mathrm{sp}} \equiv \Gamma_{\sigma,-\sigma} - \Gamma_{\sigma,\sigma}$, with $\Gamma_{\sigma,-\sigma} = -\frac{\delta\Sigma_\sigma}{\delta\mathcal{G}_{-\sigma}}$ and $\Gamma_{\sigma,\sigma} = -\frac{\delta\Sigma_\sigma}{\delta\mathcal{G}_\sigma}$, while the irreducible vertex in the charge channel Γ^{ch} is defined as $\Gamma^{\mathrm{ch}} \equiv \Gamma_{\sigma,-\sigma} + \Gamma_{\sigma,\sigma}$.

The ansatz (2) and the equations of motion for Eq. (1) lead to the following approximate relation between the two-particle density-density correlation function (double occupancy) and the single-particle self-energy and Green's function,

$$
\Sigma_{l\bar{b};\sigma\bar{\sigma}'}(z_1, \bar{z})\mathcal{G}_{\bar{b}m;\bar{\sigma}'\sigma}(\bar{z}, z_2)
$$
$$
\simeq -iU(z_1)\frac{\langle \hat{n}_{l,-\sigma}(z_1)\hat{n}_{l,\sigma}(z_1)\rangle}{\langle \hat{n}_{l,-\sigma}(z_1)\rangle\langle \hat{n}_{l,\sigma}(z_1)\rangle}(\mathcal{G}_{ll;-\sigma}(z_1, z_1^+)
$$
$$
\times \mathcal{G}_{lm;\sigma}(z_1, z_2) - \mathcal{G}_{ll;\sigma}(z_1, z_1^+)\mathcal{G}_{lm;-\sigma\sigma}(z_1, z_2)), \quad (3)
$$

where, from now on, identical contour-ordered variables and indices featuring an overline are integrated/summed over, and Latin subscripts represent lattice sites. The angular brackets denote the grand-canonical ensemble average $\langle \cdots \rangle \equiv \frac{1}{\mathcal{Z}}\sum_i \langle\Psi_i|\mathcal{T}_\mathcal{C} e^{-i\int_\mathcal{C} \mathrm{d}\bar{z}\hat{\mathcal{H}}(\bar{z})} \cdots |\Psi_i\rangle$, with $\mathcal{T}_\mathcal{C}$ the time-ordering operator on $\mathcal{C}$, $\{|\Psi_i\rangle\}$ a set of states spanning the Fock space, and $\mathcal{Z} = \sum_i \langle\Psi_i|e^{-i\int_\mathcal{C} \mathrm{d}\bar{z}\hat{\mathcal{H}}(\bar{z})}|\Psi_i\rangle$ the partition function. The last term in Eq. (3) appears in the presence of a transversal source field [39]. The interaction $U(z)$ is a function on the contour $\mathcal{C}$ that is related to $U(t)$ in Eq. (1) as follows: on the imaginary-time branch $U(z) = U(t = 0^-)$ is the interaction in the initial equilibrium state, whereas on the real-time branches $U(z) = U(t) \; \forall \; t \geqslant 0$. Equation (3) becomes exact when the substitutions $z_2 \to z_1^+$ and $m \to l$ are made.

Using the definition of Γ^{sp} it follows from Eq. (3) that

$$
i\Gamma^{\mathrm{sp}}(z) = U(z)\frac{\langle \hat{n}_{-\sigma}(z)\hat{n}_\sigma(z)\rangle}{\langle \hat{n}_{-\sigma}(z)\rangle\langle \hat{n}_\sigma(z)\rangle}. \quad (4)
$$

The irreducible vertices in both the spin and charge channels obey the local sum rule for two-particle correlation functions

$$
i\int_{-\pi}^\pi \frac{\mathrm{d}^D q}{(2\pi)^D}\, \chi_{\mathbf{q}}^{\mathrm{sp/ch}}(z, z^+)
$$
$$
= n(z) + 2(-1)^l\langle \hat{n}_{-\sigma}(z)\hat{n}_\sigma(z)\rangle - (1-l)n(z)^2, \quad (5)
$$

where $n = \langle \hat{n}_\uparrow + \hat{n}_\downarrow\rangle$ is the density of particles, $l = 0$ for charge (ch), and $l = 1$ for spin (sp). The spin (charge) susceptibility is denoted by $\chi^{\mathrm{sp(ch)}}$. The susceptibilities obey the Bethe-Salpether equation

$$
\chi_{\mathbf{q}}^{\mathrm{sp/ch}}(z, z') = \chi_{\mathbf{q}}^0(z, z')
$$
$$
+ (-1)^{l+1}\frac{i}{2}\chi_{\mathbf{q}}^0(z, \bar{z})\Gamma^{\mathrm{sp/ch}}(\bar{z})\chi_{\mathbf{q}}^{\mathrm{sp/ch}}(\bar{z}, z'), \quad (6)
$$

where χ^0 is the noninteracting susceptibility

$$
\chi_{\mathbf{q}}^0(z, z') = -2i\int_{-\pi}^\pi \frac{\mathrm{d}^D k}{(2\pi)^D}\, \mathcal{G}_{\mathbf{k}}^0(z, z')\mathcal{G}_{\mathbf{k}+\mathbf{q}}^0(z', z). \quad (7)
$$

Equations (4)–(7) self-consistently fix Γ^{sp}. Once Γ^{sp} is known, Γ^{ch} can be determined using Eqs. (5) and (6), since knowing Γ^{sp} fixes the double occupancy via Eq. (4). To satisfy the local-time sum rules (5) at a given time step, we change the argument of the local vertices integrated over in the Bethe-Salpether equation (6) from $\bar{z}$ to z, which is an approximation.

Using generating functionals with source fields $\phi_{\sigma,\sigma'}(z, z')$ and the equations of motion for Eq. (1), one can compute the second-level approximation $\Sigma^{(1)}$ to the self-energy [18]. By approximating the vertices composing $\Sigma^{(1)}$ as fully local [40],

$$
\Gamma_{l,m;i,j}(z_1, z_2; z_3, z_4) \sim \Gamma_m(z_2)\delta_\mathcal{C}(z_2, z_1)\delta_\mathcal{C}(z_2, z_3)
$$
$$
\times \delta_\mathcal{C}(z_2^+, z_4)\delta_{l,m}\delta_{l,i}\delta_{l,j}, \quad (8)
$$

$\Sigma^{(1)}$ becomes [41]

$$
\Sigma_{\mathbf{k}}^{(1)}[\alpha](z, z') = U(z)n(z)\delta_\mathcal{C}(z, z') + \frac{U(z)}{8}\int_{-\pi}^\pi \frac{\mathrm{d}^D q}{(2\pi)^D}\alpha(z')
$$
$$
\times \left[3\Gamma^{\mathrm{sp}}(z')\chi_{\mathbf{q}}^{\mathrm{sp}}(z', z) + \Gamma^{\mathrm{ch}}(z')\chi_{\mathbf{q}}^{\mathrm{ch}}(z', z)\right]
$$
$$
\times \mathcal{G}_{\mathbf{k}+\mathbf{q}}^0(z, z'), \quad (9)
$$

where the one-time variable α has been introduced to satisfy the sum rule involving the double occupancy appearing in Eq. (3),

$$
\frac{-i}{2}\int_{-\pi}^\pi \frac{\mathrm{d}^D k}{(2\pi)^D}\left[\Sigma_{\mathbf{k},\bar{\sigma}}^{(1)}[\alpha](z, \bar{z})\mathcal{G}_{\mathbf{k},\bar{\sigma}}[\Sigma^{(1)}](\bar{z}, z^+)\right]
$$
$$
= U(z)\langle \hat{n}_{-\sigma}(z)\hat{n}_\sigma(z)\rangle. \quad (10)
$$

Equation (9) preserves the crossing symmetry, that is the symmetry under the exchange of two particles or two holes. Hence, Eq. (9) is a symmetrized version of the self-energies computed in the longitudinal ($\phi_{\sigma,\sigma}$) and transverse ($\phi_{\sigma,-\sigma}$) particle-hole channels.

We note that Eq. (5) which fixes $\Gamma^{\mathrm{sp/ch}}$ is time-local, while Eq. (10) which determines α involves a convolution on the contour. This results in a qualitatively different time evolution of the two quantities. It is also important to mention that reinserting $\mathcal{G}[\Sigma^{(1)}]$ into Eq. (7) and iterating until convergence improves the energy conservation on the real-time axis, but makes the TPSC procedure violate sum rules, even though this violation is small [15,17,18,42]. The latter self-consistent method has been coined TPSC+GG [15]. The sum rule (10) is enforced for TPSC as well as for TPSC+GG at each iteration.

We now summarize the steps in the calculation of the self-energy (9), which are understood to apply to all components of the two-time functions on the KB contour. (i) Compute the noninteracting susceptibility (7) from a noninteracting Green's function $\mathcal{G}^0$ whose chemical potential matches the desired electronic density n. Note that the chemical potentials for $\mathcal{G}^0$ (μ_0) and $\mathcal{G}$ (μ) are different, but the difference $\mu - \mu_0$ is compensated by the change of the real part of the retarded self-energy at the Fermi surface $\Re\Sigma^R(\mathbf{k}_F, \omega = \mu)$ [18]. (ii) Simultaneously solve the Bethe-Salpether equation (6) for the spin channel ($l = 1$), the local sum rule (5) for the spin channel, and Eq. (4). Those three equations translate into a root-finding problem: within a time-stepping scheme, we solve for Γ^{sp} at each new maximum contour-time z using a multidimensional Newton-Raphson method for nonlinear systems of equations. This determines $\Gamma^{\mathrm{sp}}(z)$, $\chi^{\mathrm{sp}}(z, z')$ and the double occupancy $\langle \hat{n}_{-\sigma}(z)\hat{n}_\sigma(z)\rangle$. (iii) With the double occupancy known, the Bethe-Salpether equation (6) for the charge channel ($l = 0$) and Eq. (5) for the charge channel are simultaneously solved to get $\Gamma^{\mathrm{ch}}(z)$ and $\chi^{\mathrm{ch}}(z, z')$, still using the time-stepping scheme and a multidimensional root-finding method. (iv) Compute $\Sigma^{(1)}(z, z')$ using Eq. (9) [in
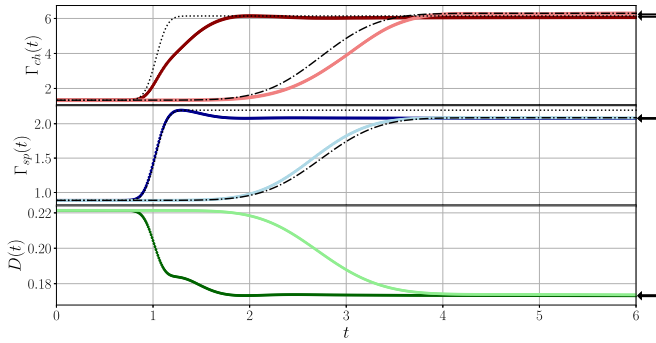
FIG. 1. Dynamics after interaction ramps from $U = 1$ to $U = 3$. The dotted and dash dotted lines show the ramp profiles in arbitrary units. The quantities plotted in light (dark) colors correspond to the slow (fast) ramp. Top panel: charge irreducible vertex $\Gamma^{\mathrm{ch}}(t)$. Middle panel: spin irreducible vertex $\Gamma^{\mathrm{sp}}(t)$. Bottom panel: Double occupancy $D(t)$. The arrows on the right indicate the thermalized values for each ramp, calculated from E_{tot} after the ramp.
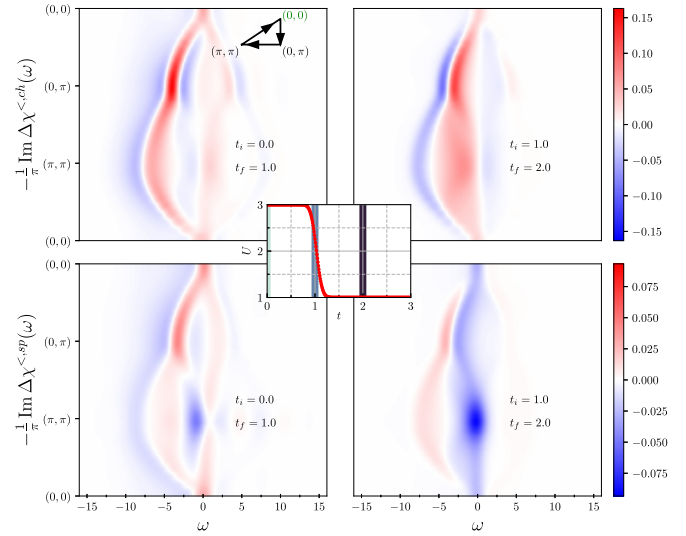

FIG. 2. Top (Bottom) panels: Difference spectra of the lesser component of the charge (spin) susceptibility after the interaction ramp shown in the inset. The inset black triangle illustrates the path in reciprocal space along which the spectra are displayed. The times t_i and t_f used in the calculation of the difference spectra are annotated in each panel. The time window used in the Fourier transformation is $\Delta t = 5$. Each row of panels uses the same color scale.

conjunction with the sum rule (10)]. TPSC+GG contains an extra loop where $\mathcal{G}[\Sigma^{(1)}]$ is reinserted into Eq. (7) and the full procedure described above is repeated until convergence. Our implementation is based on the NESSi library [43] and uses the irreducible Brillouin zone for integrals in reciprocal space [44].

Results. We apply nonequilibrium TPSC+GG to the half-filled 2D Hubbard model (1) to study the dynamics induced by interaction ramps. The corresponding TPSC results can be found in the Supplemental Material (SM) [45] (see also Refs. [42,46] therein). As a first illustration, we show in Fig. 1 the evolution of the spin ($\Gamma^{\mathrm{sp}}(t)$) and charge ($\Gamma^{\mathrm{ch}}(t)$) vertices, as well as the double occupation $D(t) = \langle n_\uparrow(t) n_\downarrow(t) \rangle$, after ramps from $U = 1$ to $U = 3$ for the initial inverse temperature $\beta = 1/T = 3$. Results are reported both for slow and fast ramps, whose profiles are indicated by the black dot-dashed and dotted lines, respectively.

In the case of the fast ramp, one notices an interesting decoupling of the dynamics of $\Gamma^{\mathrm{sp}}(t)$ and $\Gamma^{\mathrm{ch}}(t)$. While $\Gamma^{\mathrm{sp}}(t)$ reacts fast to the change in U — the spin vertex grows on the timescale set by the ramp — there is a clear delay in the growth of Γ^{ch}. In the case of Γ^{sp}, the fast response and fast relaxation after the ramp can be explained by Eq. (4): the right-hand side is proportional to $U(t)$, the denominator is constant, and $D(t)$ changes only slightly (by about 10%). After the fast ramp, the double occupation continues to decrease up to $t \approx 1.8$, which produces the overshooting of Γ^{sp}. After $t \approx 2$, the double occupation is thermalized and thus also Γ^{sp} reaches a constant value. On the other hand, for Γ^{ch}, the small change of the double occupation after the ramp still produces [via Eqs. (5) and (6)] a substantial increase. The different quantities reach a plateau at large t whose value only slightly depends on the ramp profile: this is because the inverse temperatures β_{th} of the thermalized systems after the fast and slow ramps do not differ much ($\beta_{\mathrm{th}} = 1.7$ and $\beta_{\mathrm{th}} = 2.1$, respectively). Only the charge vertex thermalized values are visibly different.

Since an interaction ramp injects an energy ΔE into the system, the temperature of the thermalized state will be higher than that of the initial state. β_{th} can be computed from the total energy of the system after the ramp. The total energy is given by the sum $E_{\mathrm{tot}}(t) = E_k(t) + E_p(t)$, with the kinetic energy $E_k(t) = \frac{-2i}{N_k} \sum_{\mathbf{k}} \epsilon_{\mathbf{k}}(t) \mathcal{G}_{\mathbf{k}}^<(t, t)$ and the potential energy $E_p(t) = \frac{-i}{N_k} \sum_{\mathbf{k}} \int_{\mathcal{C}} dz [\Sigma_{\mathbf{k}}(t, z) \mathcal{G}_{\mathbf{k}}(z, t)]^<$ [47], where $\epsilon_{\mathbf{k}}$ is the square lattice dispersion and we evaluate the sums with $N_k = 30 \times 30$ $\mathbf{k}$-points. Since $E_{\mathrm{tot}}(t)$ is almost conserved after the ramp, this allows us to compute β_{th} by searching for the β of the thermal system with the post-ramp U and energy $E_{\mathrm{tot}}(0) + \Delta E$. The black arrows in Fig. 1 show the thermalized values for the slow ramp (those for the fast ramp are almost indistinguishable). The good agreement between thermal reference data and the long-time values demonstrates that the TPSC dynamics captures the relatively fast thermalization of local quantities after the ramps.

In Fig. 2 we show the $\mathbf{k}$-resolved time evolution of the spin and charge susceptibilities. Plotted are the imaginary parts of the lesser components of the time differences $\Delta \chi(t_f, t_i, \omega) \equiv \chi(t_f, \omega) - \chi(t_i, \omega)$ for the charge (top panels) and spin (bottom panels) susceptibilities. The initial inverse temperature is $\beta = 3$. The profile of the ramp from $U = 3$ to $U = 1$, with inflection point at $t = 1$, is illustrated in the middle inset of Fig. 2. The left panels show the difference between $t_f = 1$ and $t_i = 0$, while the right panels show the difference between $t_f = 2$ and $t_i = 1$ (data for a ramp from $U = 1$ to $U = 3$ are shown in the SM). The result for $\Delta \chi^{\mathrm{ch}}$ implies a renormalization of the dispersive features which can be explained by the reduced broadening of the density of states with decreasing U. During the ramp, one observes spectral weight near $\omega \simeq 0$ with maximum intensity around $\mathbf{k} = (\pi, \pi)$ and a two-peak structure with inverted weight around $\mathbf{k} = (0, \pi)$, which indicates the transient appearance of low-energy charge excitations. As expected for a ramp to small U,
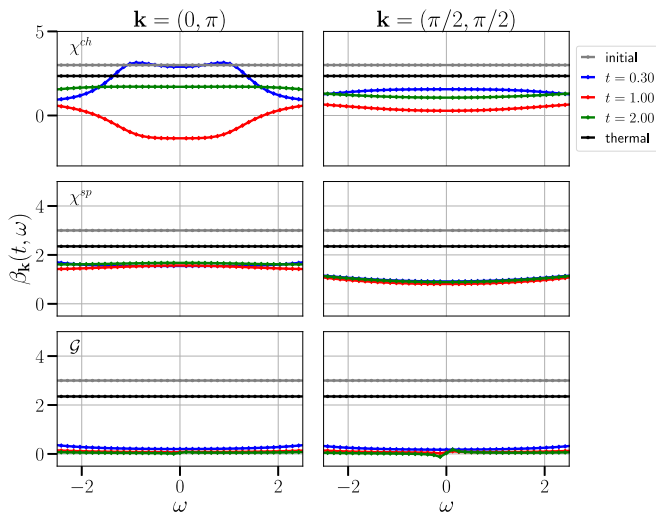
FIG. 3. Effective inverse temperatures $\beta_{\mathbf{k}}(t, \omega)$ for the Fermi momenta $\mathbf{k} = (0, \pi)$ (left panels) and $\mathbf{k} = (\frac{\pi}{2}, \frac{\pi}{2})$ [see Eq. (11)]. The gray curve plots the initial $\beta = 3$, the blue curve $\beta_{\mathbf{k}}(t = 0.3, \omega)$, the red curve $\beta_{\mathbf{k}}(t = 1, \omega)$, the green curve $\beta_{\mathbf{k}}(t = 2, \omega)$, and the black curve the thermalized value $\beta_{\mathrm{th}} = 2.35$. The top panels show the effective inverse temperatures extracted from χ^{ch}, the middle panels for χ^{sp}, and the bottom panels for $\mathcal{G}$.

the charge susceptibility approaches the result for the simple bubble (Lindhard function) [48]. The bottom panels of Fig. 2 show that the ramp from $U = 3$ to 1 mainly affects the spin excitations around $\mathbf{k} = (\pi, \pi)$, where the spectral weight is strongly reduced. This is expected since the combined effect of the reduced U and the heating suppresses the antiferromagnetic correlations. Both in the charge and spin susceptibility, the larger spectral change is observed in the second half of the ramp. In the SM, we also show the TPSC+GG equilibrium spectra for $U = 1$ and $U = 3$ at $\beta = 3$, the evolution of the single-particle spectra, as well as analogous $\mathbf{k}$-resolved time difference maps for the TPSC scheme.

As a third illustration of the nonequilibrium TPSC method, we study the thermalization of the one- and two-particle quantities $\mathcal{G}$, χ^{ch}, and χ^{sp}, and ask to what extent an effective temperature of the nonequilibrium state can be defined. For this purpose, we introduce a frequency and momentum dependent $\beta_{\mathbf{k}}(t, \omega)$ measured at time t by the formula [35]

$$\beta_{\mathbf{k}}(t, \omega) = \frac{1}{\omega} \ln \left[\mp \frac{\mathcal{A}_{\mathbf{k}}^R(t, \omega)}{\mathcal{A}_{\mathbf{k}}^<(t, \omega)} \pm 1 \right], \qquad (11)$$

which in equilibrium reduces to the inverse temperature of the system. In Eq. (11), the upper (lower) sign holds for bosonic (fermionic) quantities. If we group $\mathcal{G}$, χ^{ch}, and χ^{sp} under Λ, then $\mathcal{A}_{\mathbf{k}}^R(t, \omega) = -\frac{1}{\pi} \Im \Lambda_{\mathbf{k}}^R(t, \omega)$ stands for the spectral function, computed with the retarded component, while $\mathcal{A}_{\mathbf{k}}^<(t, \omega) = \frac{1}{2\pi} \Im \Lambda_{\mathbf{k}}^<(t, \omega)$ [49].

In Fig. 3, we plot $\beta_{\mathbf{k}}(t, \omega)$ for $\mathbf{k} = (0, \pi)$ (left panels) and $\mathbf{k} = (\frac{\pi}{2}, \frac{\pi}{2})$ (right panels) before the interaction ramp ($t = 0$), when the interaction starts changing ($t = 0.3$), during the ramp ($t = 1$), after the ramp ($t = 2$), and in the thermalized state. The interaction ramp profile is the one depicted in Fig. 2. Interestingly, for the two Fermi momenta, one finds that while a nonequilibrium temperature can be defined by Eq. (11), in

the sense that $\beta_{\mathbf{k}}(t, \omega)$ varies slowly with ω near $\omega = 0$, all three quantities exhibit different nonequilibrium temperatures and different relaxations towards the thermal value. For $\mathbf{k} = (0, \pi)$, the charge susceptibility displays a negative temperature in the middle of the interaction ramp ($t = 1$) around $\omega = 0$, which is related to the short-lived transient charge excitations with inverted weight near $\omega \simeq 0$ seen in Fig. 2. For $\mathbf{k} = (\frac{\pi}{2}, \frac{\pi}{2})$, the charge susceptibility does not yield negative effective β for the times considered, although the result for $t = 1$ corresponds to a high effective temperature and displays a significant ω-dependence. At $t = 1$ and later, for both Fermi momenta, the charge susceptibility effective temperature becomes almost ω-independent and slowly approaches the thermal value. The spin susceptibility shows a positive $\beta_{\mathbf{k}}(t, \omega)$ for all intermediate times ($t = 0.3, 1, 2$) and an even slower relaxation. At $t = 2$, the charge and spin susceptibilities yield comparable inverse temperatures for given $\mathbf{k}$, but the results differ between the two momenta. The $\beta_{\mathbf{k} = (\frac{\pi}{2}, \frac{\pi}{2})}(t, \omega)$ and $\beta_{\mathbf{k} = (0, \pi)}(t, \omega)$ extracted from the one-body Green's function correspond to very high effective temperatures, which increase up to $t = 2$. The slow thermalization of $\mathcal{G}_{\mathbf{k}}$ near the Fermi level in weakly correlated systems is expected and has already been discussed in Refs. [27,50].

Conclusions. We presented two variants of a promising method for treating nonlocal correlations in two- and higher-dimensional nonequilibrium systems, the nonequilibrium TPSC and TPSC+GG approaches. In equilibrium, these approximate methods yield remarkably accurate results in the intermediate-correlation regime [15] and they satisfy the Mermin-Wagner theorem [18] (see Ref. [51]). We explained the implementation on the Kadanoff-Baym contour and applied these methods to interaction ramps in the 2D Hubbard model. Fast perturbations induce qualitatively different dynamics in the spin and charge channels, but the local vertices and double occupation thermalize within a few inverse hopping times. Transient low-energy charge excitations corresponding to a negative effective temperature in the charge sector can appear during the ramp. While the effective temperatures extracted from the charge and spin susceptibilities and single-particle Green's function are relatively well defined in frequency space, they differ substantially from each other and depend on the momentum, which shows that a unique nonequilibrium temperature of a strongly perturbed weakly interacting system cannot be defined within a few hopping times after a ramp. How exactly the different effective temperatures approach the thermal value in the weak- and intermediate-correlation regime is an interesting subject for further studies, which, however, requires the implementation of memory truncation techniques [52–54] and compact basis representations [55] to access the long-time dynamics.

Extensions of nonequilibrium TPSC which build in nonperturbative local correlations from DMFT [5,56,57] should capture strong correlation effects and could provide access to Mott physics. Since TPSC can tackle multi-orbital [21,56] and extended-Hubbard [16] model systems, we believe that TPSC (and DMFT+TPSC) combined with time-dependent Density Functional Theory input [22,58] will provide a promising and computationally tractable path towards realistic simulations of photoexcited correlated materials.

[1] G. Rohringer, H. Hafermann, A. Toschi, A. A. Katanin, A. E. Antipov, M. I. Katsnelson, A. I. Lichtenstein, A. N. Rubtsov, and K. Held, Rev. Mod. Phys. **90**, 025003 (2018).

[2] D. Bergeron, V. Hankevych, B. Kyung, and A.-M. S. Tremblay, Phys. Rev. B **84**, 085128 (2011).

[3] A. Kauch, P. Pudleiner, K. Astleithner, P. Thunström, T. Ribic, and K. Held, Phys. Rev. Lett. **124**, 047401 (2020).

[4] O. Simard, S. Takayoshi, and P. Werner, Phys. Rev. B **103**, 104415 (2021).

[5] H. Kusunose, J. Phys. Soc. Jpn. **75**, 054713 (2006).

[6] T. Maier, M. Jarrell, T. Pruschke, and M. H. Hettler, Rev. Mod. Phys. **77**, 1027 (2005).

[7] A. Georges, G. Kotliar, W. Krauth, and M. J. Rozenberg, Rev. Mod. Phys. **68**, 13 (1996).

[8] A. Toschi, A. A. Katanin, and K. Held, Phys. Rev. B **75**, 045118 (2007).

[9] A. Rubtsov, M. Katsnelson, and A. Lichtenstein, Ann. Phys. **327**, 1320 (2012).

[10] L. Hedin, Phys. Rev. **139**, A796 (1965).

[11] H. Fukuyama and Y. Hasegawa, Prog. Theor. Phys. Suppl. **101**, 441 (1990).

[12] N. Bickers and D. Scalapino, Ann. Phys. **193**, 206 (1989).

[13] J. Gukelberger, L. Huang, and P. Werner, Phys. Rev. B **91**, 235114 (2015).

[14] K. Van Houcke, E. Kozik, N. Prokof'ev, and B. Svistunov, Phys. Procedia **6**, 95 (2010).

[15] T. Schäfer, N. Wentzell, F. Šimkovic, Y.-Y. He, C. Hille, M. Klett, C. J. Eckhardt, B. Arzhang, V. Harkov, F.-M. Le Régent, A. Kirsch, Y. Wang, A. J. Kim, E. Kozik, E. A. Stepanov, A. Kauch, S. Andergassen, P. Hansmann, D. Rohe, Y. M. Vilk *et al.*, Phys. Rev. X **11**, 011058 (2021).

[16] B. Davoudi and A.-M. S. Tremblay, Phys. Rev. B **74**, 035113 (2006).

[17] Y. M. Vilk, L. Chen, and A.-M. S. Tremblay, Phys. Rev. B **49**, 13267 (1994).

[18] Y. M. Vilk and A.-M.S. Tremblay, J. Phys. I France **7**, 1309 (1997).

[19] B. Kyung, V. Hankevych, A.-M Daré, and A.-M. S. Tremblay, Phys. Rev. Lett. **93**, 147004 (2004).

[20] B. Kyung, J.-S. Landry, and A.-M. S. Tremblay, Phys. Rev. B **68**, 174502 (2003).

[21] K. Zantout, S. Backes, and R. Valentí, Ann. Phys. **533**, 2000399 (2021).

[22] S. Bhattacharyya, K. Björnson, K. Zantout, D. Steffensen, L. Fanfarillo, A. Kreisel, R. Valentí, B. M. Andersen, and P. J. Hirschfeld, Phys. Rev. B **102**, 035109 (2020).

[23] M. Balzer and M. Potthoff, Phys. Rev. B **83**, 195132 (2011).

[24] C. Jung, A. Lieder, S. Brener, H. Hafermann, B. Baxevanis, A. Chudnovskiy, A. Rubtsov, M. Katsnelson, and A. Lichtenstein, Ann. Phys. **524**, 49 (2012).

[25] D. Golež, L. Boehnke, H. U. R. Strand, M. Eckstein, and P. Werner, Phys. Rev. Lett. **118**, 246402 (2017).

[26] D. Golež, M. Eckstein, and P. Werner, Phys. Rev. B **100**, 235117 (2019).

[27] O. Simard, M. Eckstein, and P. Werner, Phys. Rev. B **104**, 245127 (2021).

[28] C. Stahl and M. Eckstein, Phys. Rev. B **103**, 035116 (2021).

[29] N. Bittner, D. Golež, M. Casula, and P. Werner, Phys. Rev. B **104**, 115138 (2021).

[30] E. Perfetto, Y. Pavlyukh, and G. Stefanucci, Phys. Rev. Lett. **128**, 016801 (2022).

[31] F. Hofmann, M. Eckstein, and M. Potthoff, J. Phys.: Conf. Ser. **696**, 012002 (2016).

[32] N. Tsuji, P. Barmettler, H. Aoki, and P. Werner, Phys. Rev. B **90**, 075117 (2014).

[33] M. Eckstein and P. Werner, Sci. Rep. **6**, 21235 (2016).

[34] N. Bittner, D. Golež, M. Eckstein, and P. Werner, Phys. Rev. B **101**, 085127 (2020).

[35] N. Bittner, D. Golež, M. Eckstein, and P. Werner, Phys. Rev. B **102**, 235169 (2020).

[36] S. Latini, E. Perfetto, A.-M Uimonen, R. van Leeuwen, and G. Stefanucci, Phys. Rev. B **89**, 075306 (2014).

[37] E. Perfetto, A.-M. Uimonen, R. van Leeuwen, and G. Stefanucci, Phys. Rev. A **92**, 033419 (2015).

[38] L. P Kadanoff and G. Baym, *Quantum Statistical Mechanics: Green's Function Methods in Equilibrium and Nonequilibrium Problems* (CRC Press, Boca Raton, 1962).

[39] S. Allen, A.-M. S. Tremblay, and Y. M. Vilk, in *Theoretical Methods for Strongly Correlated Electrons*, edited by D. Sénéchal, C. Bourbonnais, and A.-M. S. Tremblay (Springer, New York, 2003).

[40] $\delta_\mathcal{C}(z, z')$ are Dirac delta functions on the contour $\mathcal{C}$ and $\delta_{r,s}$ are Kronecker deltas.

[41] D. Sénéchal, A.-M. S. Tremblay, and C. Bourbonnais, *Theoretical Methods for Strongly Correlated Electrons* (Springer, New York, 2004).

[42] Y. M. Vilk and A.-M. S. Tremblay, Europhys. Lett. **33**, 159 (1996).

[43] M. Schüler, D. Golez, Y. Murakami, N. Bittner, A. Herrmann, H. Strand, P. Werner, and M. Eckstein, Comput. Phys. Commun. **257**, 107484 (2020).

[44] J. J. Jorgensen, J. E. Christensen, T. J. J. null, and G. L. W. Hart, Commun. Comput. Phys. **31**, 495 (2022).

[45] See Supplemental Material at http://link.aps.org/supplemental/10.1103/PhysRevB.106.L241110 for complementary equilibrium benchmarks found in the literature as well as further nonequilibrium results for TPSC and TPSC+GG.

[46] J. Kanamori, Prog. Theor. Phys. **30**, 275 (1963).

[47] The potential energy can also be obtained from Eq. (5). The results are consistent within numerical accuracy.

[48] V. H. Dao and R. Frésard, Phys. Rev. B **95**, 165127 (2017).

[49] H. Aoki, N. Tsuji, M. Eckstein, M. Kollar, T. Oka, and P. Werner, Rev. Mod. Phys. **86**, 779 (2014).

[50] M. Moeckel and S. Kehrein, Phys. Rev. Lett. **100**, 175702 (2008).

[51] While a global temperature cannot be defined in a nonequilibrium state, the nonequilibrium distribution function tends

to have a finite slope [27], which means that the (energy-dependent) effective temperature is nonzero. Therefore, we do not expect the appearance of long-range order in nonequilibrium states for dimension $D \leqslant 2$.

[52] C. Stahl, N. Dasari, J. Li, A. Picano, P. Werner, and M. Eckstein, Phys. Rev. B **105**, 115146 (2022).

[53] M. Schüler, M. Eckstein, and P. Werner, Phys. Rev. B **97**, 245129 (2018).

[54] J. Yin, Y.-H. Chan, F. H. da Jornada, D. Y. Qiu, S. G. Louie, and C. Yang, J. Computat. Sci., **64**, 101843 (2022).

[55] J. Kaye and D. Golež, SciPost Phys. **10**, 091 (2021).

[56] K. Zantout, S. Backes, A. Razpopov, D. Lessnich, and R. Valenti, arXiv:2211.01400.

[57] N. Martin, C. Gauvin-Ndiaye, and A. M. S. Tremblay, arXiv:2211.01919.

[58] E. Runge and E. K. U. Gross, Phys. Rev. Lett. **52**, 997 (1984).